



**CHALMERS**  
UNIVERSITY OF TECHNOLOGY

## **Investigating Load-dependent Wear Behavior and Degradation Mechanisms in Cr<sub>3</sub>C<sub>2</sub>-NiCr coatings deposited by HVAF and HVOF**

Downloaded from: <https://research.chalmers.se>, 2024-03-13 07:28 UTC

Citation for the original published paper (version of record):

Mahade, S., Mulone, A., Bjorklund, S. et al (2021). Investigating Load-dependent Wear Behavior and Degradation Mechanisms in Cr<sub>3</sub>C<sub>2</sub>-NiCr coatings deposited by HVAF and HVOF. Journal of Materials Research and Technology, 15: 4595-4609.  
<http://dx.doi.org/10.1016/j.jmrt.2021.10.088>

N.B. When citing this work, cite the original published paper.



Available online at [www.sciencedirect.com](http://www.sciencedirect.com)  
**jmr&t**  
 Journal of Materials Research and Technology  
 journal homepage: [www.elsevier.com/locate/jmrt](http://www.elsevier.com/locate/jmrt)



## Original Article

# Investigating load-dependent wear behavior and degradation mechanisms in $\text{Cr}_3\text{C}_2$ –NiCr coatings deposited by HVOF and HVOF



Satyapal Mahade<sup>a,\*</sup>, Antonio Mulone<sup>b</sup>, Stefan Björklund<sup>a</sup>, Uta Klement<sup>b</sup>, Shrikant Joshi<sup>a</sup>

<sup>a</sup> Department of Engineering Science, University West, Trollhättan, Sweden

<sup>b</sup> Department of Industrial and Materials Science, Chalmers University of Technology, Gothenburg, Sweden

## ARTICLE INFO

### Article history:

Received 25 September 2021

Accepted 19 October 2021

Available online 23 October 2021

### Keywords:

Ball-on-disc test

$\text{Cr}_3\text{C}_2$ –NiCr

Wear

High velocity air fuel (HVOF)

High velocity oxy-fuel

## ABSTRACT

Wear resistant coatings that comply with non-toxic environment goals are highly desirable.  $\text{Cr}_3\text{C}_2$ –NiCr is a promising alternative to the toxic, 'Co'-containing WC–Co coatings to mitigate wear. The purpose of this study was to examine the suitability of  $\text{Cr}_3\text{C}_2$ –NiCr coatings for automotive brake disc application by systematically investigating their dry sliding wear behavior at different test conditions. Therefore, High Velocity Air Fuel (HVOF) and High Velocity Oxy Fuel (HVOF) were employed to deposit  $\text{Cr}_3\text{C}_2$ –NiCr coatings. The powder feedstock and as-deposited  $\text{Cr}_3\text{C}_2$ –NiCr coatings were characterized for their microstructure and phase composition using SEM and XRD. Mechanical properties (hardness, fracture toughness), porosity and surface topography of the as-deposited coatings were evaluated. The coatings were subjected to sliding wear tests at different normal loads (5 N, 10 N and 15 N) using alumina ball as the counter surface. Coefficient of friction (CoF) evolution of HVOF and HVOF deposited coatings, along with their wear performance, was obtained for different normal load conditions. The wear performance ranking of HVOF and HVOF processed coatings was influenced by the test conditions, with HVOF coatings demonstrating better wear resistance than HVOF coatings at harsh test conditions and the HVOF coatings performing better under mild wear test conditions. Detailed post-wear analysis of worn coatings, the alumina ball counter-body and the resulting debris was performed to reveal the degradation mechanisms at different test conditions. Findings from this work provide new insights into the desirable microstructural features to mitigate wear, which can be further exploited to deposit wear-resistant coatings.

© 2021 The Author(s). Published by Elsevier B.V. This is an open access article under the CC BY license (<http://creativecommons.org/licenses/by/4.0/>).

\* Corresponding author.

E-mail address: [satyapal.mahade@hv.se](mailto:satyapal.mahade@hv.se) (S. Mahade).

<https://doi.org/10.1016/j.jmrt.2021.10.088>

2238-7854/© 2021 The Author(s). Published by Elsevier B.V. This is an open access article under the CC BY license (<http://creativecommons.org/licenses/by/4.0/>).

## 1. Introduction

Durability and performance of several engineering components is often compromised due to wear-related degradation [1,2]. Different metallic, ceramic and cermet-based protective coatings are often employed to combat wear [3–7]. Among the existing list of coating compositions to mitigate wear, WC–Co coatings possess superior wear resistance [8–10] and are consequently widely used in applications such as automotive brake discs [4]. However, ‘Co’ is known to be carcinogenic [11], which exposes the operators and end-users to health hazard [12]. Furthermore, ‘Co’ is not an economically viable and sustainable option due to its limited availability worldwide [13]. Therefore, Co-free coating compositions that possess adequate wear resistance are highly desirable in order to comply with sustainability and non-toxicity standpoints.

Cr<sub>3</sub>C<sub>2</sub>-based cermet coatings have demonstrated excellent wear performance at high temperature [14–16], and established themselves as promising contenders to replace the toxic, ‘Co’-containing WC–Co coatings. Among the Cr<sub>3</sub>C<sub>2</sub>-based coatings, Cr<sub>3</sub>C<sub>2</sub> (75)–NiCr (25) is the most widely utilized coating composition to mitigate wear of industrial components [17]. In particular, for automotive brake disc applications, coatings that are resistant to sliding wear are of interest in order to comply with the norms laid down by the European Commission with respect to particulate emissions of matter <10 µm [18]. Therefore, investigating room temperature sliding wear behavior of Cr<sub>3</sub>C<sub>2</sub> (75)–NiCr (25) is of immense industrial interest, especially for assessing their suitability as a wear-resistant coating for applications such as automotive brake disc.

In the past, extensive work was reported on room temperature sliding wear behavior of thermally sprayed Cr<sub>3</sub>C<sub>2</sub> (75)–NiCr (25) coatings [17,19–22]. The sliding wear performance of fine feedstock derived Cr<sub>3</sub>C<sub>2</sub>(75)–NiCr(25) coatings was shown to be promising due to homogeneous distribution of carbides in the matrix [20]. Bolelli et al. reported improved sliding wear performance (lower CoF and lower wear rate) of Cr<sub>3</sub>C<sub>2</sub>–NiCr coatings processed utilizing fine feedstock due to the fine wear debris generation [17]. Additionally, incorporation of a softer NiCrBSi as lubricating phase in the Cr<sub>3</sub>C<sub>2</sub>(75)–NiCr(25) feedstock did not lower the coefficient of friction [23]. Annealing of Cr<sub>3</sub>C<sub>2</sub> (75)–NiCr (25) coatings has led to conflicting results, with Gariboldi et al. [24] reporting enhancement in wear performance and Guilemany et al. [25] finding deterioration in tribological behavior under sliding wear conditions.

Different processing techniques such as laser cladding [26], PVD [27], CVD [28], and thermal spray [29,30] are often employed to manufacture wear-resistant coatings for industrial applications. Among these techniques, thermal spray is an attractive route to economically coat industrial components without being constrained by the component size [4,30,31]. Atmospheric plasma spray (APS) [32,33], High velocity oxy-fuel (HVOF) [17] and High velocity air fuel (HVOF) [17] processing routes have been employed in the past to deposit Cr<sub>3</sub>C<sub>2</sub>–NiCr coatings. However, plasma processed carbide-based coatings are prone to decarburization due to their relatively higher processing temperature compared to

HVOF and HVOF [34,35]. Therefore, HVOF and HVOF processes have gained immense academic and industrial interest to deposit wear-resistant coatings [4,29].

In view of the acknowledged promise of the above high-velocity methods, extensive studies have been reported on sliding wear performance comparison of HVOF and HVOF processed WC-based coatings at different normal loads [36–38]. Bolelli et al. [16] and Matikainen et al. [17] investigated the temperature dependent sliding wear performance of Cr<sub>3</sub>C<sub>2</sub>–NiCr coatings processed via HVOF and HVOF. Although a handful of studies investigated the sliding wear of plasma sprayed Cr<sub>3</sub>C<sub>2</sub>–NiCr coatings at different normal loads [33], a systematic investigation of load dependent-wear performance has not been conducted yet for HVOF and HVOF processed Cr<sub>3</sub>C<sub>2</sub>–NiCr coatings. The Cr<sub>3</sub>C<sub>2</sub>–NiCr coatings are of immense industrial interest due to their excellent wear performance and non-toxic nature as they are free from the carcinogenic ‘Co’-binder. Therefore, novelty of this work was to shed light on the load-dependent dry sliding wear performance and wear mechanisms of HVOF and HVOF processed Cr<sub>3</sub>C<sub>2</sub> (25)–NiCr (25) coatings. The rationale for opting 25 wt.% Ni(Cr) binder content and 75 wt.% carbide content was their optimum hardness and sliding wear performance [39]. The Cr<sub>3</sub>C<sub>2</sub> (75)–NiCr (25) coatings were deposited using standard HVOF and HVOF parameters and detailed microstructure examination, topography studies and phase analysis were performed. The HVOF and HVOF processed Cr<sub>3</sub>C<sub>2</sub>–NiCr coatings were subjected to ball-on-disc tests at three different normal loads (5 N, 10 N and 15 N) using an alumina ball as the counter material. The specific wear rates and the evolution of the coefficient of friction were compared for the HVOF and HVOF processed coatings under different normal load conditions. Comprehensive post wear analysis of the coatings the mating alumina ball, and wear debris was performed using SEM/EDS to reveal wear mechanisms.

## 2. Experimental work

Carbon steel substrates of disc geometry (25.4 mm diameter and 6 mm thickness) were grit blasted using alumina of 220-grit size to achieve a surface roughness of approximately 3 µm (Ra). The grit blasted surfaces were cleaned with pressurized air to remove any loosely bound particles, including grit media. A commercially available, agglomerated and sintered chromium carbide (75)-nickel chromium (25) powder (Cr<sub>3</sub>C<sub>2</sub>–NiCr, Amperit 588.059, Höganäs Germany GmbH) with a particle size distribution of D<sub>10</sub> 9–13 µm, D<sub>50</sub> 18–24 µm and D<sub>90</sub> 30–44 µm was used as the feedstock to deposit coatings. An M3 (UniqueCoat, U.S) torch was used to deposit Cr<sub>3</sub>C<sub>2</sub>–NiCr coatings via HVOF process using standard spray parameters. Similarly, standard HVOF spray parameters developed by TSE AB, Malmö, Sweden were used to deposit Cr<sub>3</sub>C<sub>2</sub>–NiCr coatings using a DiamondJet torch (Oerlikon Metco, USA) and 5MPE-HP feeding system (Sulzer Metco, Germany). The spray parameters used for depositing HVOF and HVOF coatings are summarized in Table 1.

Surface topography of the as-deposited coatings was analyzed using RTS optical profiler (Wyko® NT1100, USA). The as-deposited coatings were sectioned, mounted and polished

**Table 1 – HVAF and HVOF processing parameters to deposit  $\text{Cr}_3\text{C}_2$ -NiCr coatings.**

Coating ID	Standoff distance (mm)	Powder feed rate (g/min)	Air pressure (psi)
HVAF coating	350	150	111
HVOF coating	250	40	390

according to the standard procedures discussed elsewhere [40]. The mirror-polished specimens were analyzed for their cross-sectional microstructures by SEM (Hitachi TM 3000, Japan and Zeiss Gemini SEM 450, Zeiss, Oberkochen, Germany). An open domain software, Image J [41], was used to analyze the porosity content of the as-deposited coatings using twenty-five independent high magnification ( $2000\times$ ) SEM micrographs. Hardness measurements were carried out with a micro-hardness tester (HVM-2 series, SHIMADZU Corp., Japan) on the polished surface of the coatings with a normal load of 0.98 N, while the fracture toughness was measured with a higher normal load of 2.94 N. Fifteen independent indents were made and their mean and standard deviation are reported. XRD analysis was performed on the top surface of the deposited coatings using a Bruker AXS D8 advance (Karlsruhe, Germany) diffractometer with Cr K $\alpha$  radiation ( $\lambda = 2.28970 \text{ \AA}$ ) operated at 40 kV and 50 mA.

The as-deposited coatings were polished to a surface roughness of  $<0.2 \text{ }\mu\text{m}$  (Ra) prior to performing sliding wear tests. Ball-on-Disc tests were performed at room temperature according to ASTM standard G-99 using Tribometer (TRB<sup>3</sup>, Anton-Paar, Netherlands). An alumina ball of 6 mm in diameter obtained from ST instruments, Netherlands, was used as the counter-material. Three different normal loads (5 N, 10 N and 15 N) were used while all other test conditions were kept unchanged (linear velocity = 0.2 m/s; sliding distance = 2500 m). Three specimens of each type of coating (HVAF and HVOF) were identically tested at every load (5 N, 10 N and 15 N). The evolution of coefficient of friction with sliding time was recorded during each test. In the post-wear analysis, volume loss of the worn coatings was measured using white light interferometry (Profilm 3D, Filmetrics, Germany) and their specific wear rates were calculated according to the following equation:

$$\text{Specific wear rate} = \frac{\text{Volume loss (mm}^3\text{)}}{\text{Normal load(N)} \times \text{sliding distance(m)}} \quad (1)$$

The worn coating surface, worn alumina ball surface and the wear debris were analyzed using SEM/EDS.

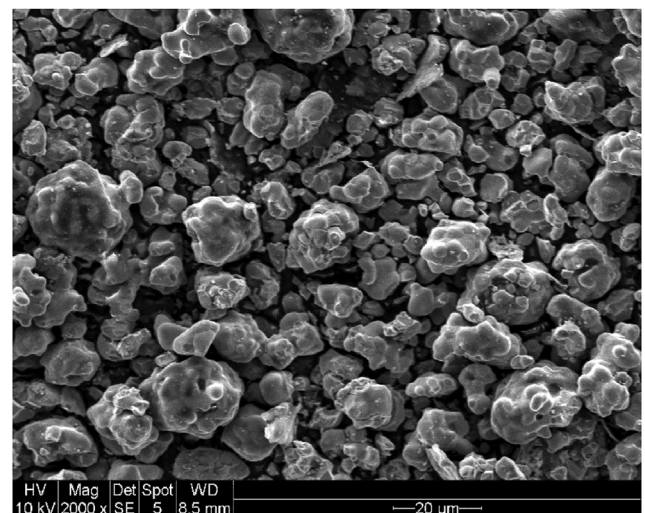
### 3. Results and discussion

#### 3.1. Microstructure

The SEM image of the  $\text{Cr}_3\text{C}_2$ -NiCr powder in Fig. 1 showed agglomerated particles in the size range of 15–20  $\mu\text{m}$ . The particle size of the powder feedstock influences the microstructure and wear behavior of thermally sprayed coatings [16]. A finer particle size ( $<5 \text{ }\mu\text{m}$ ) is undesirable for HVOF

spraying of powder feedstock, as they have a high surface area to volume ratio and a low weight, which leads to poor flowability and a loss in deposition efficiency [42]. In addition, a finer feedstock tends to overheat and lead to thermally induced phase transformations [42,43] in case of cermets such as  $\text{Cr}_3\text{C}_2$ -NiCr, which have large difference in melting point of carbide phase and the metallic binder phase. According to Fig. 1, the  $\text{Cr}_3\text{C}_2$ -NiCr powder feedstock used in this study contains only few fine-sized particles.

The cross-sectional SEM micrograph of the HVAF sprayed  $\text{Cr}_3\text{C}_2$ -NiCr coating showed a delamination-free interface with the substrate according to Fig. 2(a). The coating microstructure was dense and showed no visible cracks within the bulk of the coating. However, few delamination cracks (as seen approximately 10  $\mu\text{m}$  from the coating surface in Fig. 2(a)) were sometimes visible at the interface of penultimate and final spray pass. This could be attributed to the lack of peening effect on the final spray pass during HVAF spraying. Typically, during polishing and grinding operations of as-deposited coatings, the surface cracks are eliminated as they are restricted to the near-surface region. The coating thickness was measured to be approximately 300  $\mu\text{m}$ . At higher magnification, SEM images of the coating cross-section showed two distinct phases (seen as light and dark gray) in Fig. 2(b). The light phase corresponds to metallic Ni-binder, while the gray phase corresponds to the hard  $\text{Cr}_3\text{C}_2$ . It can also be seen that the carbide phase was irregular shaped and plastically undeformed whereas the metallic binder appears to be plastically deformed. Pores were also evident in the cross-section image in Fig. 2(b). The SEM micrograph of the surface at low magnification in Fig. 2(c) showed a dense microstructure. A closer examination of the surface at higher magnification in Fig. 2(d) showed two well-distributed, distinct areas; one of them flattened to an extent, while the other did not appear to have undergone any deformation and had a particle-like appearance. Typically, in HVAF spraying, the ductile feedstock undergoes plastic deformation upon impact with the substrate [44]. In addition, depending on the processing

**Fig. 1 – SEM analysis of the  $\text{Cr}_3\text{C}_2$ -NiCr feedstock.**



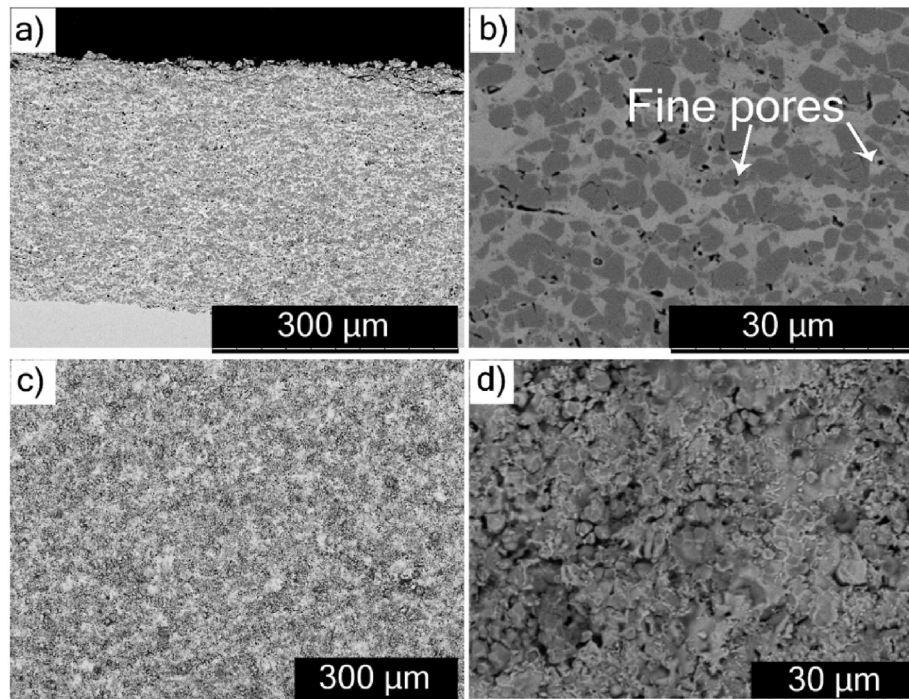


**Fig. 2 – SEM analysis of HVAF sprayed  $\text{Cr}_3\text{C}_2$ –NiCr coating: (a & b) cross-section (c & d) top surface.**

conditions, the feedstock may partially melt during flight before it is deposited [45]. In the present case, the ductile metallic Ni-matrix plastically deforms and accommodates the brittle ceramic ( $\text{Cr}_3\text{C}_2$ ) phase. Therefore, in Fig. 2(d), the

particle-like phase corresponds to carbides, while the flattened phase corresponds to the Ni-matrix.

In the case of the HVOF sprayed coating, the SEM image of the cross-section in Fig. 3(a) showed a similar

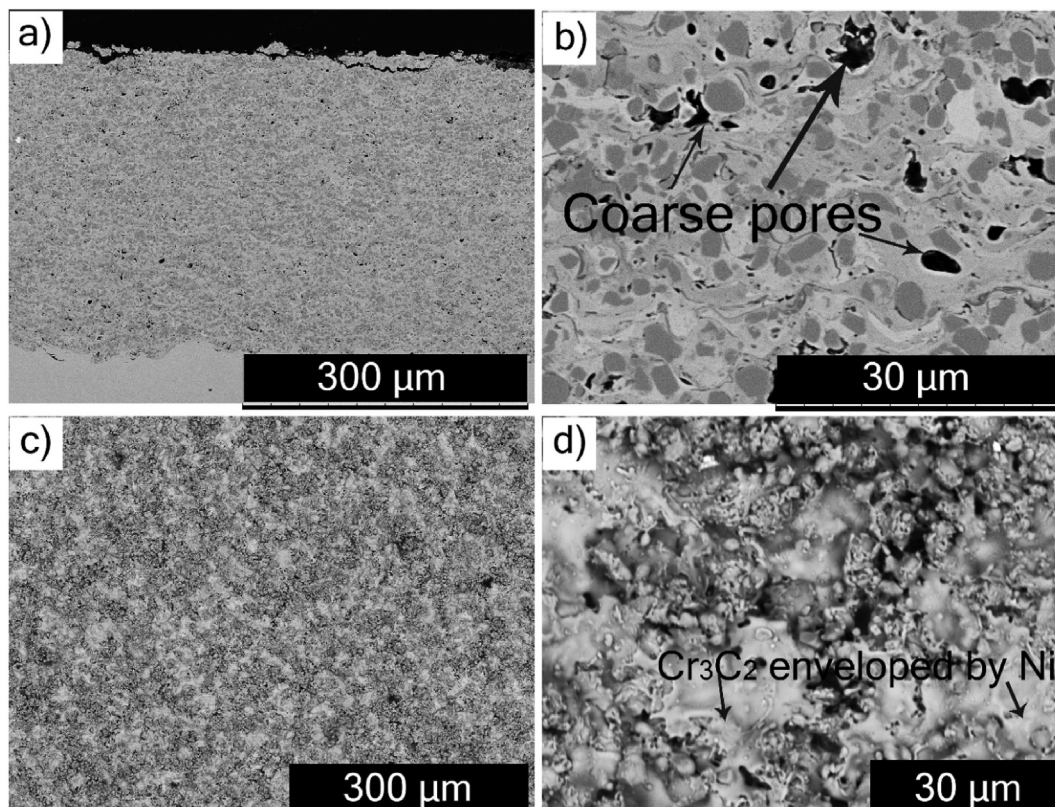


**Fig. 3 – SEM analysis of HVOF sprayed  $\text{Cr}_3\text{C}_2$ –NiCr coating: (a & b) cross-section and (c & d) surface.**

microstructure to that of HVOF coating, in which a defect-free interface with the substrate was achieved. Even a near-surface delamination crack was also observed in the HVOF coated specimen, see Fig. 3(a). The coating thickness was approximately 300  $\mu\text{m}$ . The high magnification SEM micrograph of the cross-section in Fig. 3(b) also showed two distinct, well-distributed, particle-like ( $\text{Cr}_3\text{C}_2$ ) gray phase along with the light 'Ni' phase. The particle-like shape of  $\text{Cr}_3\text{C}_2$  indicates that HVOF spraying too was unable to accomplish complete melting of carbides in the feedstock during flight. In addition, pores can be seen in Fig. 3 (b) which were larger compared to the HVOF spray coating. In dry unlubricated wear applications, porosity is known to be undesirable and can adversely affect durability and performance [45,46]. The SEM micrograph of the surface also showed similarities with the HVOF sprayed coating, with a dense coating surface being observed, see Fig. 3(c). The high magnification SEM image of the surface of the HVOF sprayed coating in Fig. 3(d) showed molten and re-solidified splats. Additionally, the carbide phase seems to be enveloped by the Ni-phase. These subtle differences in microstructural features for HVOF and HVOF coatings could potentially influence the respective sliding wear performance and the applicable degradation mechanisms.

### 3.2. Surface topography

The surface roughness of the as-deposited coatings was measured using an optical profiler and 2D representations of the surface roughness are shown in Fig. 4. As shown in Fig. 4, a slightly higher surface roughness ( $S_a$  in  $\mu\text{m}$ ) was measured for the HVOF sprayed coatings. The higher roughness of HVOF coatings could be related to particle-like carbides in the microstructure that appear to protrude from the surface of the coating, as seen in Fig. 2(d). On the other hand, as previously observed in Fig. 3(d), in the HVOF coating, the carbide phase was enveloped by the molten and re-solidified Ni-matrix that appeared to be flattened to a greater extent, resulting in its lower surface roughness compared to HVOF coating. It should be mentioned that, for wear applications, a lower surface roughness of the as-deposited coating is often desired in order to save time and costs associated with grinding and polishing operations when mating surfaces are involved in actual application.

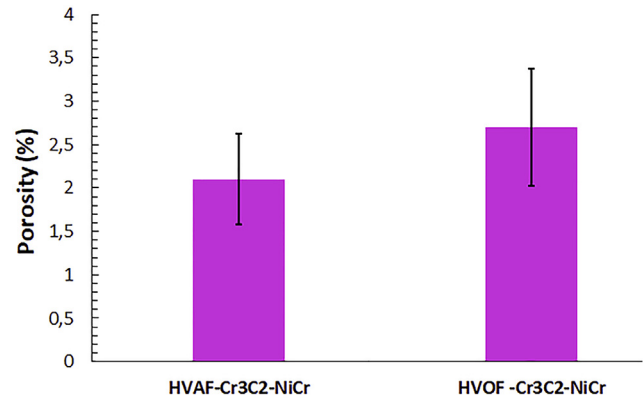


Fig. 5 – Porosity content of HVOF and HVOF sprayed  $\text{Cr}_3\text{C}_2$ -NiCr coatings.

### 3.3. Porosity analysis

Porosity content of the HVOF and HVOF deposited coatings was comparable after considering the uncertainty in measurement, as shown in Fig. 5. The results of the SEM analysis in the previous section show that the pore size in the HVOF spray coating was larger ( $\sim 3\text{--}4\ \mu\text{m}$ ) than the pores size ( $< 2\ \mu\text{m}$ ) in HVOF coating, according to Figs. 2(b) and 3(b). For dry wear applications, porosity is undesirable as it acts as the weaker link in the coating and results in inferior mechanical properties and wear performance [47]. In addition, homogeneously distributed pores with a smaller pore size are generally desirable, since the wear degradation sites are localized and relatively pronounced in coatings with larger pores [48].

### 3.4. XRD analysis

XRD analyses were performed on the  $\text{Cr}_3\text{C}_2$ -NiCr feedstock powder and on the as-sprayed coatings and the results are shown in Fig. 6. The XRD results show that both as-sprayed coatings retain the crystalline phases present in the feedstock powder, i.e. a Ni-based phase and the  $\text{Cr}_3\text{C}_2$  phase. However, the peaks of the metallic phase appear broader in the sprayed coatings than the peak in the feedstock powder. The observed broadening can be related to phase amorphization during spraying. In fact, previous studies have

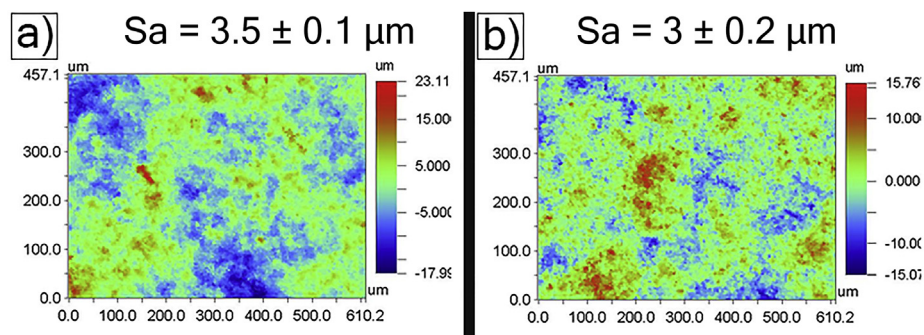


Fig. 4 – 2D representation of the surface roughness of the  $\text{Cr}_3\text{C}_2$ -NiCr coating deposited by a) HVOF b) HVOF.



suggested that the rapid solidification occurring after HVOF spraying of  $\text{Cr}_3\text{C}_2\text{-NiCr}$  coatings can result in the amorphization of the metallic matrix [49,50]. On the other hand, in the case of HVAF sprayed  $\text{Cr}_3\text{C}_2\text{-NiCr}$  coatings, the formation of an amorphous metallic phase is mainly related to the severe plastic deformation of the feedstock upon impact with the substrate [16]. Despite the difference in processing conditions, a comparable phase composition is observed for HVAF and HVOF processed  $\text{Cr}_3\text{C}_2\text{-NiCr}$  coatings. In addition, neither decarburization of the carbide phase nor any formation of new phases can be seen in the two investigated coatings.

### 3.5. Mechanical properties

Micro-indentation was used to characterize the as-deposited HVAF and HVOF sprayed coatings. In general, a micro-indentation technique estimates the mechanical properties from a localized area and may not represent the mechanical properties of the entire (global) coating [51]. Although micro-indentation technique may not provide an accurate estimate of absolute mechanical properties, it is a reliable technique for ranking the mechanical properties of thermally sprayed coatings [47] and, consequently, widely utilized to evaluate hardness, fracture toughness, etc. [52,53].

Hardness of the HVAF sprayed coating was slightly higher than the HVOF sprayed coating, according to Fig. 7(a). In general, differences in hardness in thermally sprayed coatings could be attributed to factors such as microstructural features, phase constitution and porosity content. In the current study, as confirmed by the XRD analysis, phase constitution of the HVAF and HVOF processed  $\text{Cr}_3\text{C}_2\text{-NiCr}$  coatings was similar. Furthermore, the porosity content of the as-deposited coatings was also comparable. However, the difference in microstructural features (pore size, etc.) discussed in the previous section could have resulted in a difference in hardness. Higher coating hardness can be beneficial in minimizing wear loss [54]. Furthermore, a higher coating fracture toughness delays the onset of crack propagation and enhances the coating's

durability when subjected to wear [55]. Although HVAF sprayed coatings exhibited higher hardness than HVOF sprayed coatings, their fracture toughness was comparable to that of corresponding HVOF coatings after considering the scatter in measurement, see Fig. 7(b).

### 3.6. Sliding wear testing

The evolution of the coefficient of friction (CoF) of HVAF and HVOF sprayed coatings at different normal loads (5 N, 10 N and 15 N) is shown in Fig. 8. The HVOF sprayed coating at 5 N load showed stable CoF after the running-in stage whereas the HVAF coating showed an increase in CoF from 0.35 to 0.75 after reaching a sliding distance of approximately 1600 m, see Fig. 8(a). Furthermore, after reaching a CoF of 0.75, the HVAF coating showed a stable value until the end of test. All the 3 test repetitions conducted for HVAF and HVOF coatings at 5 N consistently showed similar CoF evolution.

The HVAF coating at 10 N load showed stable CoF values in the steady state-regime whereas the HVOF sprayed coatings showed slightly higher CoF than the HVAF coating along with fluctuation in the CoF in the steady-state regime. A similar trend was observed on increasing the normal load to 15 N. Stable CoF values for the HVAF coating in the steady state regime can be observed, while fluctuation in CoF was noted in case of the HVOF coating in the steady regime, see Fig. 8(c). It should be mentioned that coatings possessing lower CoF can aid in lowering the wear rates [56,57]. Although an identical powder feedstock was utilized to deposit HVAF and HVOF coatings that led to comparable porosity content and phase composition, the difference in CoF evolution with applied

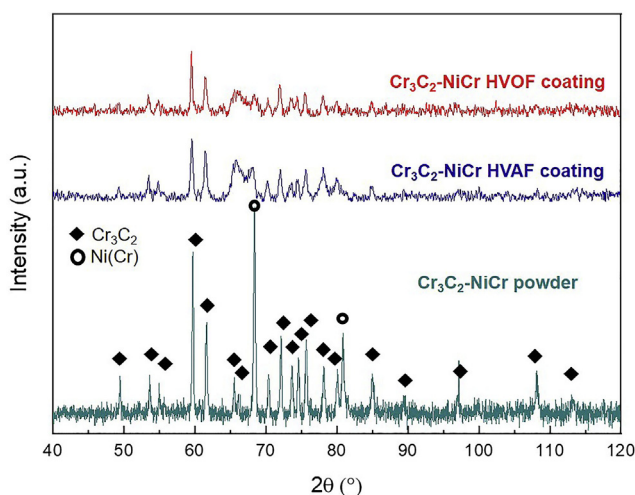


Fig. 6 – XRD analysis of  $\text{Cr}_3\text{C}_2\text{-NiCr}$  feedstock and of the as-deposited HVAF and HVOF processed  $\text{Cr}_3\text{C}_2\text{-NiCr}$  coatings.

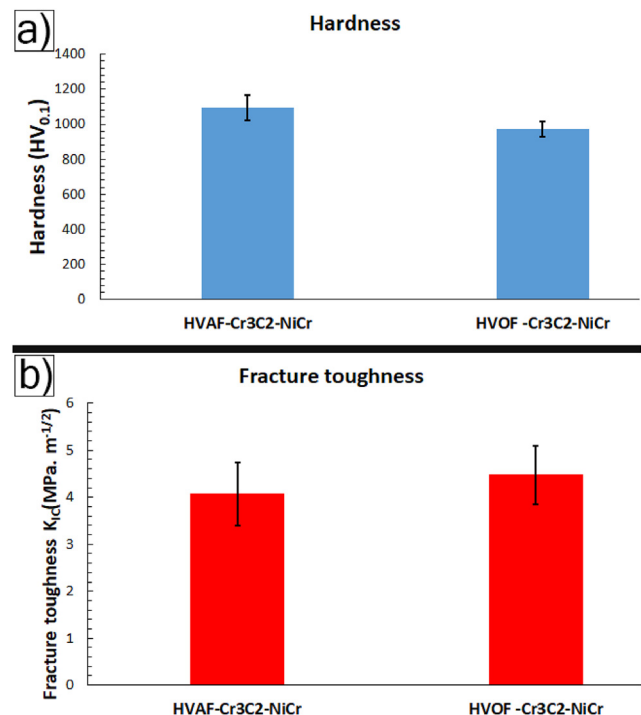
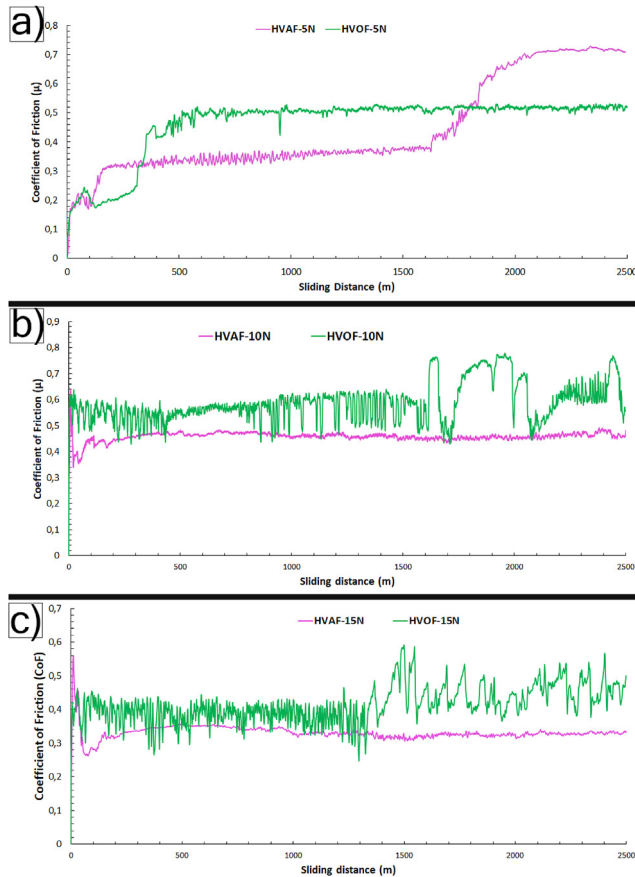


Fig. 7 – Mechanical properties of HVAF and HVOF processed  $\text{Cr}_3\text{C}_2\text{-NiCr}$  coatings: a) hardness b) fracture toughness.



**Fig. 8 – Sliding distance vs. coefficient of friction of HVAF and HVOF sprayed coatings at different normal loads a) 5 N b) 10 N c) 15 N.**

normal load is not well understood. Therefore, a detailed post-mortem analysis of the worn coatings, wear debris and the counter surface was performed to shed light on the differences in wear behavior along with the wear mechanisms prevailing in the investigated coatings.

The specific wear rates of HVAF and HVOF sprayed  $\text{Cr}_3\text{C}_2$ -NiCr coatings evaluated at different normal loads (5 N, 10 N and 15 N) are shown in Fig. 9. The HVAF sprayed coating showed inferior wear resistance at lower load (5 N) compared to HVOF coating. However, at 10 N normal load, the ranking

was reversed and the HVAF coating showed higher wear resistance than HVOF sprayed coating. Additionally, the specific wear rate for HVAF coating at different normal loads of 5 N and 10 N was comparable, while that of the HVOF coating increased substantially. With further increase in normal load to 15 N, the specific wear rates of both the HVAF and HVOF sprayed coatings increased substantially compared to those observed at 10 N load. The HVOF sprayed coatings showed significantly higher specific wear rates than the corresponding HVAF sprayed coatings at higher normal loads (10 N and 15 N). Additionally, the HVAF and HVOF sprayed coatings showed comparable porosity content and fracture toughness. However, the HVAF and HVOF sprayed coatings exhibited different microstructural features such as larger pore size for HVOF coatings, and the substantially covered carbide phase by the Ni-phase in HVOF sprayed coatings. Furthermore, the HVAF sprayed coating showed slightly higher hardness than the HVOF sprayed coatings. These differences could have led to the noted difference in their wear performance, as discussed in detail in the subsequent section.

### 3.7. Post-wear analysis

#### 3.7.1. Lower normal load (5 N)

The worn surface of the HVOF coating after testing at a load of 5 N showed a wear track width of approximately  $440\ \mu\text{m}$ , see Fig. 10(a). The wear track also showed a dark phase. The micro-cutting action of trapped wear particles on the coating surface was also evident from the abrasion marks in Fig. 10(b), indicating abrasive wear mechanism. Adhesive wear scars, denoted by a circle, can also be seen in the coating's wear track in Fig. 10(b). The higher magnification SEM micrograph of the wear track in Fig. 10(c) along with the corresponding EDS elemental maps confirmed the dark phase to be 'O' rich, indicating the formation of tribo-oxides. Furthermore, the absence of 'Al' in the coatings' wear track confirms that no material transfer from the ball surface to the coated specimen occurred.

The SEM/EDS analysis of debris collected after wear testing of the HVOF coating at a load of 5 N showed a distribution of large ( $\sim 15\ \mu\text{m}$ ) and small ( $< 3\ \mu\text{m}$ ) wear particles, according to Fig. 11. The elemental maps confirmed the presence of 'Al', 'Ni', 'Cr' and 'O', indicating that the debris originated from material loss from both the alumina ball surface and the

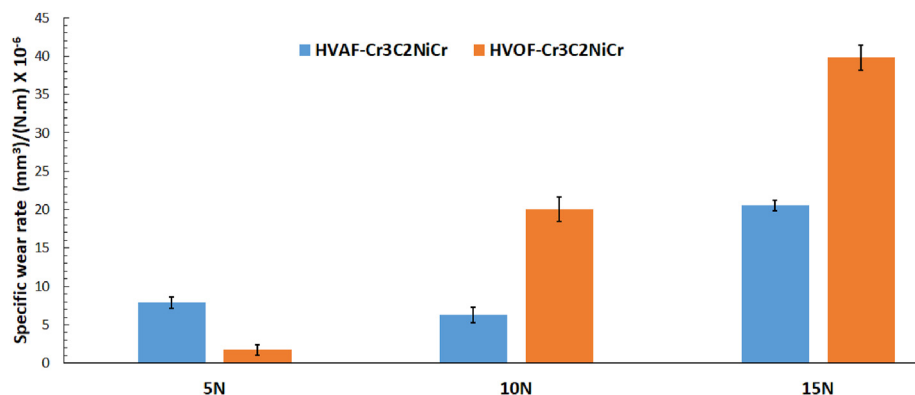


**Fig. 9 – Specific wear rates of the HVAF and HVOF sprayed  $\text{Cr}_3\text{C}_2$ -NiCr coatings at different normal loads.**



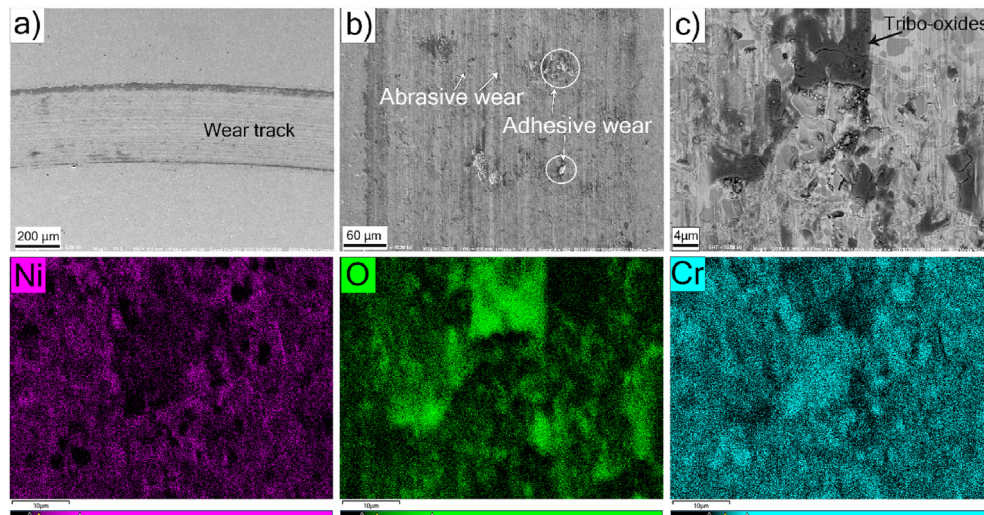


**Fig. 10** – SEM/EDS analysis of worn HVOF coating: a) micrograph showing wear track b) micrographs showing abrasive and adhesive wear scars c) micrograph showing tribo-oxides and their corresponding elemental maps.

coating. Furthermore, the larger wear particles seem to be generated due to adhesive wear resulting from cold junction between alumina/tribo-oxides (Cr and Ni-oxide) as the larger wear particle comprised 'Al', 'Ni', 'Cr' and 'O'.

In the case of the HVAF coating, a larger wear track width (~470 μm) than for the HVOF coating was observed, according to Fig. 12(a). Additionally, in contrast to the HVOF coating, the SEM image in Fig. 12(a) showed an extensive presence of dark phase (tribo-oxides) in the entire wear track, see Fig. 10(a). As shown in Fig. 12(a) and (b), the formed tribo-oxide layer seems to have spalled-off near the center of the wear track and shows the brighter (Ni matrix) and greyish (carbide) phases underneath. The spallation/detachment of the tribo-oxide can plausibly explain the sudden spike in the coefficient of friction observed after ~1600 m of sliding distance, see Fig. 8(a). SEM/EDS analysis of the wear track shown in Fig. 12(c) confirmed the presence of O, Cr and Ni in the dark phase, indicating tribo-oxidation as one of the wear mechanisms. The wear track in Fig. 12(c) also showed micro-cutting of the Ni-matrix and micro-cracking of the carbide phase due to the trapped wear particles between the coating/alumina surfaces, due to which the abrasive wear mechanism comes into play.

Furthermore, the tribo-oxide film formed in the wear track of the coating during the sliding wear test showed visible cracks that were randomly oriented, according to Fig. 12(c). Typically, the wear particles generated from the coating/counter surface during the test are trapped between the mating surfaces, which are fragmented into finer particles during the course of the test [45]. These fine wear particles oxidize due to frictional heat generated during the test and are eventually smeared onto the surface of coating/alumina ball [44,58]. The formation of such tribo-oxides during wear tests has been reported to aid in lowering CoF and minimizing the wear rate [45]. However, the influence of tribo-oxides on the coating's wear performance depends on several factors such as the test conditions (applied load, linear speed, etc.), composition of the tribo-oxide, adhesion of the tribo-oxide film to the surface, tribo-oxide thickness etc. [59].

The SEM/EDS analysis of debris generated from sliding wear testing of the HVAF coating showed cluster of particles that were less than 6 μm in size, according to Fig. 13. The elemental maps of the wear debris confirmed the presence of Al, Ni, Cr, O, indicating material loss from the alumina ball surface and the coating. Furthermore, the debris generated

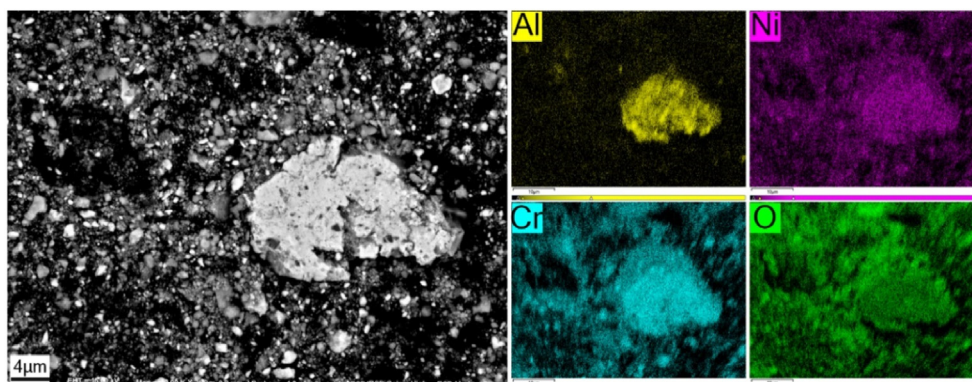


**Fig. 11** – SEM/EDS analysis of the wear debris of the HVOF coating after ball-on-disc testing at a normal load of 5 N.

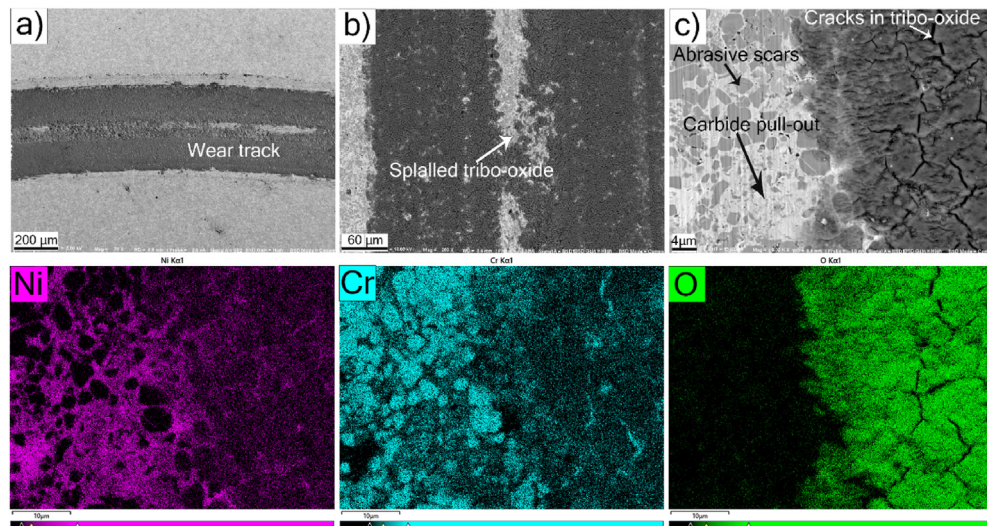


**Fig. 12 – SEM/EDS analysis of the worn HVOF coating after ball-on-disc testing at a load of 5 N a) micrograph of wear track b) micrograph showing spalled tribo-oxide layer c) micrograph showing carbide pullout, cracks in tribo-oxide layer along with the corresponding elemental maps.**

from the coating were mostly tribo-oxides as the elemental maps of 'Cr' and 'Ni' revealed that these elements co-existed with a corresponding 'O' map.

The ball wear scars of HVOF and HVOF tested coatings at different normal load conditions are shown in Fig. 14. The alumina ball used as a counter surface with the HVOF coated specimen showed an elliptical scar with minor axis of approximately 300 μm, see Fig. 14(a). One possible explanation for the elliptical wear scar noted on the ball can be the accumulation of wear debris in the vicinity of the contact region between the coating and the ball. On the other hand, the alumina ball used for the HVOF coated specimen showed a mildly distorted circular wear scar with a diameter of approximately 280 μm, see Fig. 14(e). This would suggest that the wear debris generated in the case of the HVOF coating gets expelled from the contact region.

The post-wear analysis of HVOF and HVOF coatings after testing at a normal load of 5 N sheds light on the respective CoF evolution discussed in the previous section. The strong tribo-oxide formation in case of the HVOF coating explains its lower CoF up to a sliding distance of 1600 m compared to the

HVOF coating. The spallation of the tribo-oxide film in the HVOF coating after a sliding distance of 1600 m led to an increase in its CoF from 0.35 to 0.75, which was higher than for the HVOF coating. On the other hand, the discrete tribo-oxides formed in the case of HVOF coating did not result in lowering its CoF. The wear debris analysis of HVOF and HVOF coatings showed similarities in terms of material loss from the alumina ball and the coating. However, the shape of the wear scar on the ball differed for the HVOF and HVOF coatings due to the interaction of wear debris generated from the coatings with the contact region. The difference in wear behavior is intimately related to the microstructural differences where the particle-like carbide phase morphology in the HVOF coating appears to easily detach from the matrix, resulting in the formation of wear particles that act as three-body abrasion media and contribute to the higher wear rate than in the HVOF coating. In the case of HVOF coating, the splat-like morphology of the binder matrix enveloped the carbide phase effectively and resisted easier detachment of  $\text{Cr}_3\text{C}_2$  and formation of three body abrasion media, resulting in lower wear rate than in the HVOF coating.

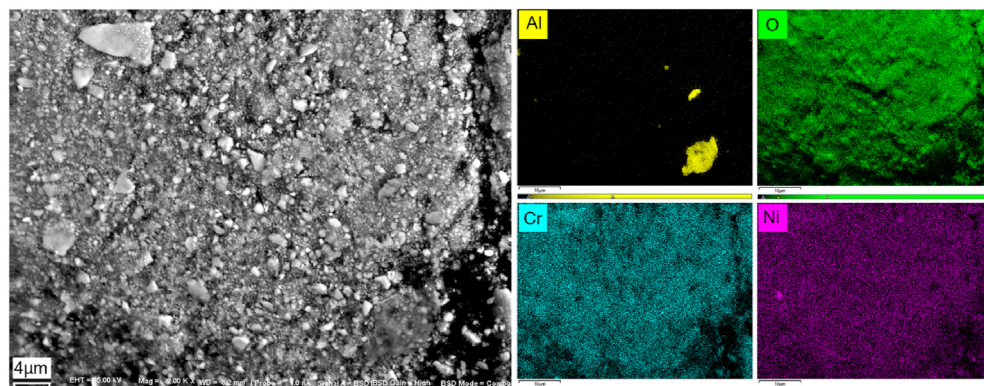


**Fig. 13 – SEM/EDS analysis of wear debris generated from the HVOF coating at 5 N normal load.**



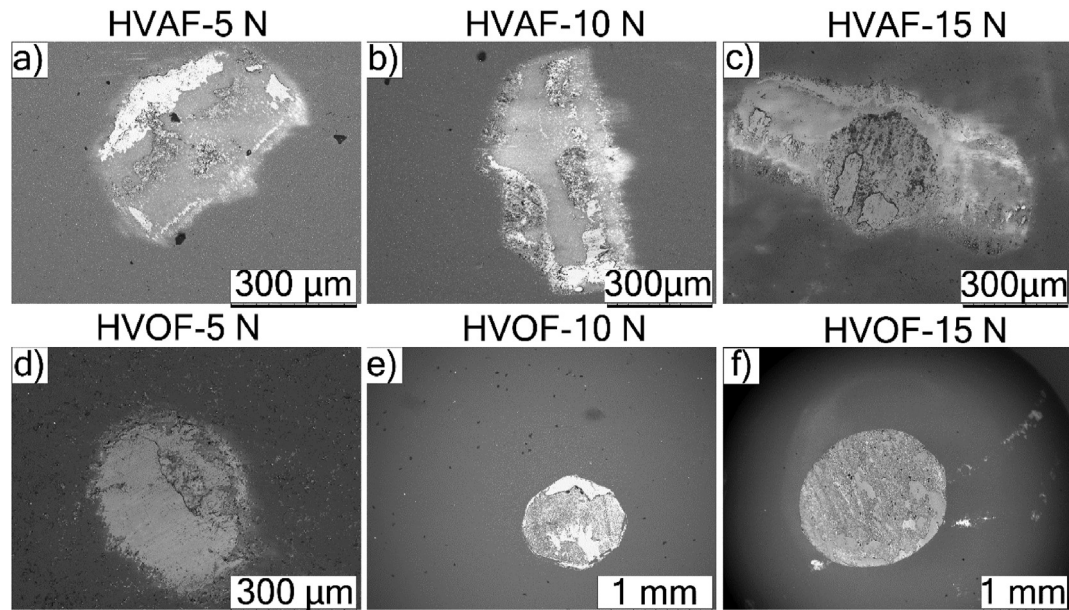


**Fig. 14** – SEM analysis of wear scars on alumina ball used as counter surface for (a, b and c) HVOF coating subjected to 5 N, 10 N and 15 N load, respectively (d, e, f) HVOF coating subjected to 5 N, 10 N and 15 N load, respectively.

### 3.7.2. Post wear analysis at 15 N normal load

The SEM analysis of the HVOF coating exposed to a 15 N normal load during wear testing showed a wear track width of approximately 2000  $\mu\text{m}$ , see Fig. 15(a). The wear track in Fig. 15(b) showed abrasive wear (micro-cutting and micro-cracking) scars along with dark phase, whose corresponding elemental maps revealed tribo-oxides (Cr, Ni & O). Additionally, elemental mapping also revealed the presence of 'Al' in the wear track, indicating material transfer from the alumina ball to the coating. Comparing HVOF coating after wear testing at 5 N and 15 N, it can be seen that an increase in normal load resulted in smearing of wear debris generated from the alumina ball on the coating surface. It should be mentioned that the wear debris trapped in the

wear track contributes to three-body abrasion, resulting in enhanced wear loss. The higher magnification SEM micrograph of the wear track in Fig. 15(c) showed local collapsing of splat, along with a network of randomly oriented cracks in its close vicinity. The reason for the collapse of splats can be attributed to the presence of coarse pores under the surface, which tend to reduce the local load-bearing capacity of the splats at higher applied loads (15 N). In the past, a similar collapse of splats due to porosity was reported at intermediate to high loads for thermally sprayed coatings [60].

SEM/EDS analysis of the wear debris revealed material loss from the coating and alumina ball, according to elemental maps of Al, Ni and Cr shown in Fig. 16. Additionally, the wear

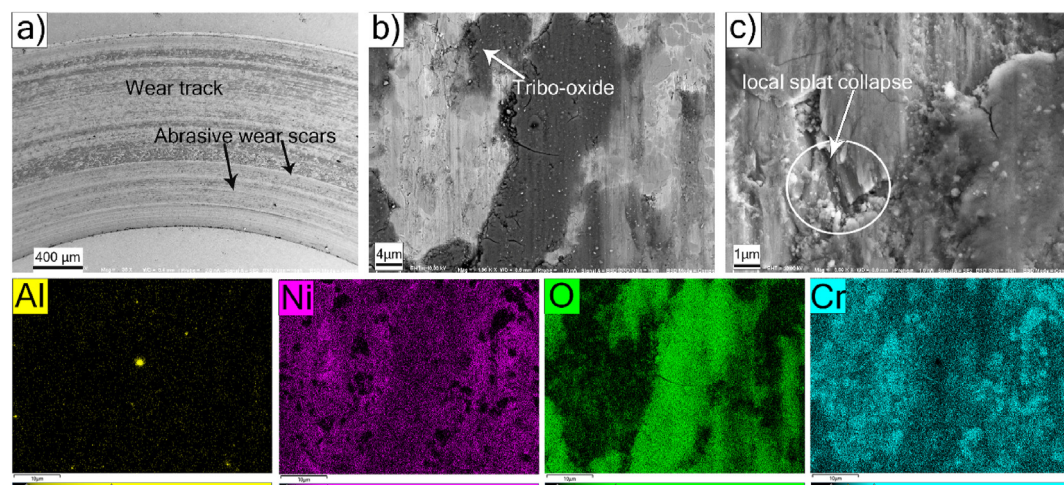


**Fig. 15** – SEM/EDS analysis of the HVOF coating subjected to sliding wear test at 15 N normal load a) low magnification of wear track b) high magnification of wear track and its corresponding elemental maps showing tribo-oxides, c) encircled region in micrograph showing local collapse of splat.

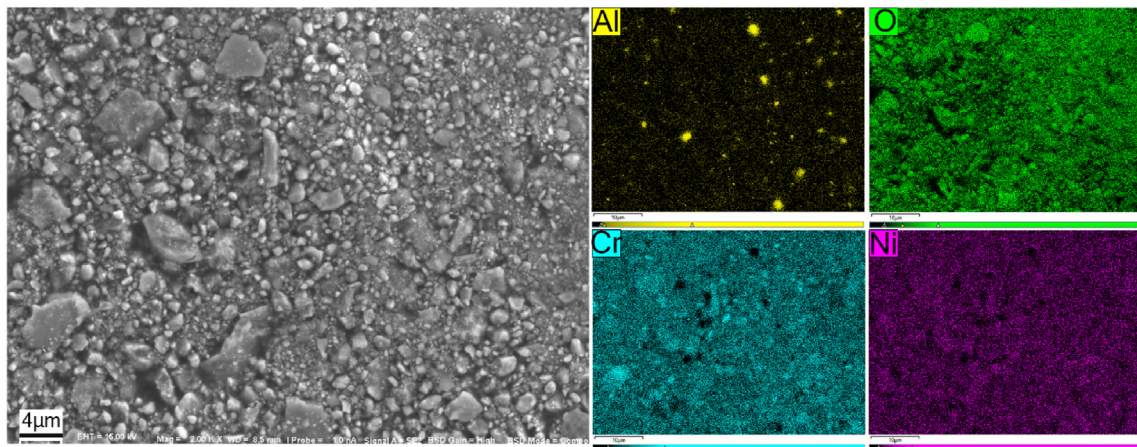


Fig. 16 – SEM/EDS analysis of the wear debris of the HVOF coating after ball-on-disc testing at 15 N normal load.

debris generated from the coating was in the form of tribo-oxides (Cr, Ni and O). The ball wear scar of the HVOF coating after a load of 15 N seen in Fig. 14(f) showed a circular shape of approximately 2 mm diameter, which correlated with the coating's wear scar width. With an increase in load from 5 N to 15 N, the diameter of the ball wear scar increased for the HVOF coating along with the retention of circular shape. Smeared tribo-oxides can also be clearly seen on the surface of the worn alumina ball.

In the case of the HVAF coating, the wear track width shown in Fig. 17(a) was approximately 1000  $\mu\text{m}$ , i.e. half of the wear track width of the HVOF coating. The wear track width ranking of HVAF and HVOF coatings subjected to a load of 15 N also correlated with their specific rate ranking at 15 N. The wear track in Fig. 17(b) also showed smeared wear particles on the coating surface that resulted in abrasive wear (micro-cutting) scars along the sliding direction. The higher magnification SEM image in Fig. 17(c) and the corresponding elemental maps (Al, Cr, Ni, O) further confirm that the wear particles generated from the alumina ball resulted in abrasive

wear in the coating. The SEM image in Fig. 17(c) also showed carbide-pullout from the worn coating surface.

The SEM/EDS analysis of the wear debris in Fig. 18 showed fine particles (<4  $\mu\text{m}$  size) that comprised mostly tribo-oxides (Cr, Ni and O) along with traces of 'Al', indicating material loss from the coating and the ball surface. The ball wear scar in Fig. 14(c) showed an elliptical shape whose major axis was approximately 1000  $\mu\text{m}$ , in contrast to the circular shaped scar observed in the case of the HVOF coating. Additionally, the wear scar showed smeared tribo-oxide layer.

### 3.8. Microstructure-wear behavior correlation

In general, the HVAF sprayed coating comprises partially molten and plastically deformed/undeformed splats due to its lower processing temperature than coatings produced by HVOF and plasma spray [29,44]. During HVAF spraying of a cermet feedstock such as  $\text{Cr}_3\text{C}_2\text{-NiCr}$ , the binder (Ni) undergoes plastic deformation upon impact and accommodates the harder carbide phase that barely undergoes any plastic

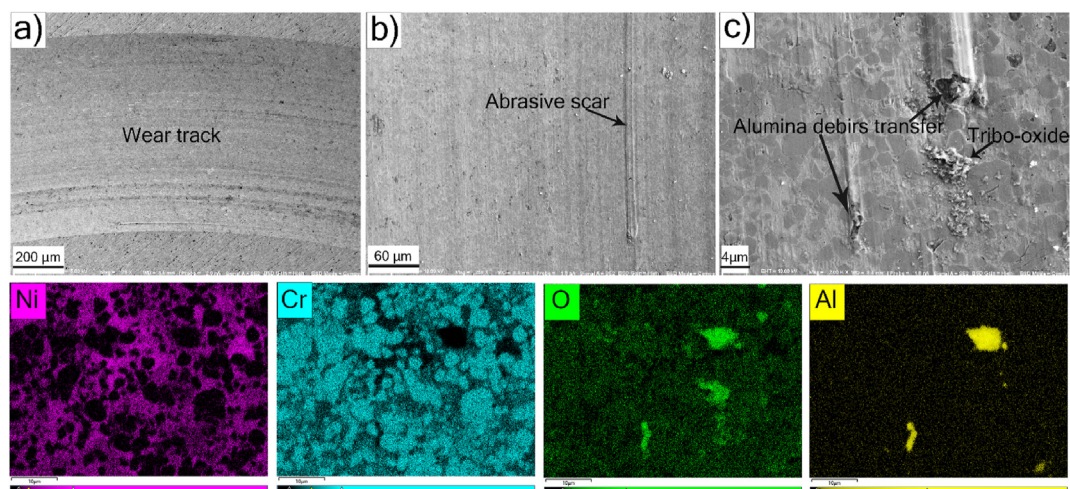


Fig. 17 – SEM/EDS analysis of HVAF coating subjected to sliding wear test at 15 N normal load a) wear track b) micrograph showing abrasive wear scars c) micrograph showing tribo-oxides in the elemental maps along with material transfer from ball to coating.



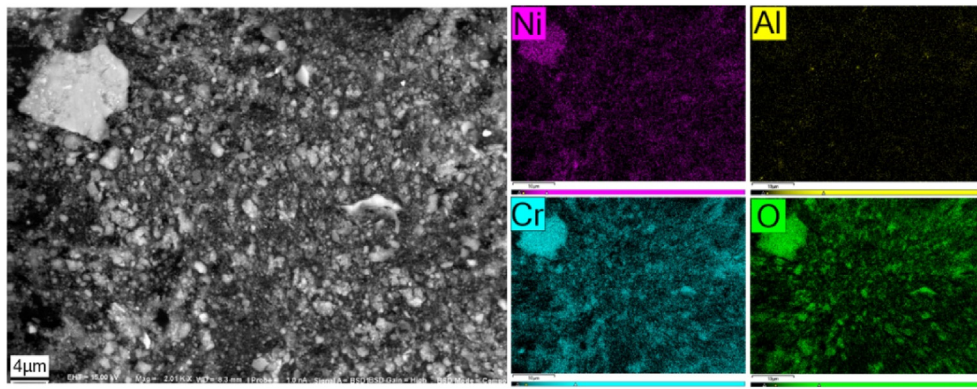


Fig. 18 – SEM/EDS analysis of the wear debris of the HVOF coating subjected to 15 N normal load.

deformation. Furthermore, porosity in a HVOF sprayed coating is formed due to inadequate plastic deformation of the binder as a result of insufficient kinetic and thermal energy imparted to the feedstock. In this work, the HVOF coating seemed to possess adequate thermal and kinetic energy that resulted in low porosity. With HVOF sprayed coatings, the feedstock underwent inflight melting due to its higher processing temperature compared to HVOF. In this study, the binder phase (Ni) melted and/or plastically deformed, which resulted in well-defined splats enveloping the harder  $\text{Cr}_3\text{C}_2$  phase by the binder (Ni) and rendering a smoother surface compared to a HVOF coating. In HVOF sprayed coatings, pores are formed when the feedstock does not undergo adequate melting or plastic deformation [30]. In the current study, HVOF coatings showed low porosity content, comparable to the porosity content of HVOF sprayed coatings. However, the pore size in the HVOF sprayed coating was larger than in the HVOF sprayed coating. XRD results also confirmed

that the phase composition of HVOF and HVOF sprayed coatings was similar and showed minimal oxidation/decarburation. Furthermore, the fracture toughness of the HVOF and HVOF coatings was comparable.

The sliding wear performance of HVOF sprayed coatings was inferior to HVOF coatings at lower normal load (5 N). The as-deposited and post wear SEM analysis indicated that the particle-like carbide phase was easily detached/pulled-out from the binder (Ni) in the case of HVOF sprayed coating. The worn carbide particles trapped in the contact region between the alumina ball and the coating and contributed to three-body abrasion, resulting in higher wear rates. The wear particles entrapped in the contact region became finer with the progression of the test and were eventually smeared onto the coating's surface as tribo-oxides. On the other hand, the splat-like appearance of the binder phase in the HVOF coating that enveloped the carbide phase resisted its detachment/pull-out, resulting in

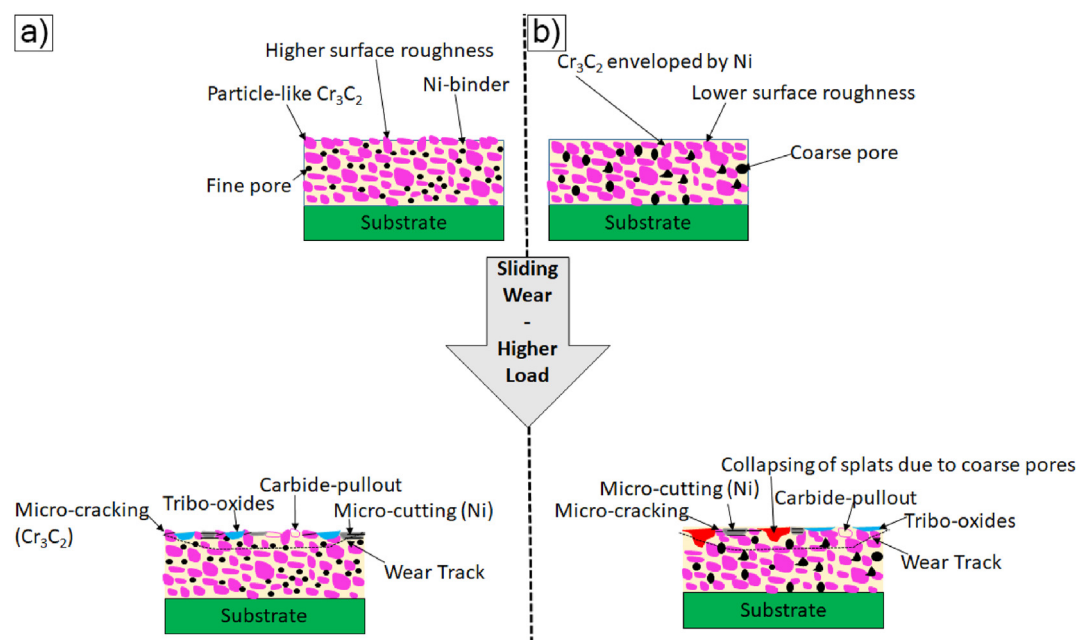


Fig. 19 – Illustration of sliding wear behavior and degradation mechanisms of  $\text{Cr}_3\text{C}_2$ -NiCr coatings deposited by a) HVOF, and b) HVOF.

superior wear resistance at lower loads. Additionally, extensive tribo-oxide formation in the case of HVAF sprayed coating due to easier detachment of  $\text{Cr}_3\text{C}_2$  particles from the matrix at 5 N load led to lower CoF than HVOF coating up to ~1600 m of sliding distance. Delamination of tribo-oxides after 1600 m of sliding distance, as evident from the post wear analysis of HVAF coating, led to abrupt spike in CoF for HVAF coating. However, at higher normal loads, the wear performance was reversed and the HVAF coating exhibited higher wear resistance than the HVOF sprayed coatings. A schematic illustration of the influence of microstructural features on the wear behavior and mechanisms at higher normal load is shown in Fig. 19. Based on the post-wear SEM/EDS analysis, it can be said that, at higher normal load (10 N and 15 N), presence of larger sub-surface pores in the HVOF sprayed coating resulted in localized collapse of splats. Additionally, the wear debris generated and entrapped in the wear track due to localized collapse of splats further contributed to wear losses via three-body abrasion. On the other hand, the relatively fine pores in HVAF coating resisted localized collapse of splats at higher load. Furthermore, the HVAF coating showed minimal tribo-oxides smeared onto the coating's surface at 15 N compared to that observed at 5 N load, indicating the applied normal load influences formation and adhesion of tribo-oxides on the surface. The results of this work on the load-dependent formation and delamination of tribo oxides agree with the results on thermally sprayed cermet coatings by Vashishtha et al. [58]. The HVAF and HVOF coatings showed similar wear mechanisms, i.e., abrasive wear (micro-cutting of Ni and micro-cracking of  $\text{Cr}_3\text{C}_2$ ), tribo-oxidation, adhesive wear, brittle-fracture of the carbides, carbide-pullout, etc., see Fig. 19. However, their distinct microstructural features appeared to dictate wear performance at different load conditions.

#### 4. Conclusion

In this work, two different thermal spray processing technologies, i.e., High Velocity Air Fuel (HVAF) and High Velocity Oxy-Fuel (HVOF), were employed to deposit  $\text{Cr}_3\text{C}_2$ -NiCr coatings utilizing previously optimized set of spray parameters. The deposited coatings were characterized in detail for their microstructure, porosity content, phase composition, mechanical properties, and surface roughness. The as-deposited coatings were subjected to ball-on-disc tests at mild (5 N, 10 N) and harsh (15 N) sliding wear conditions. The important findings from this work can be summarized as follows:

- Surface morphology of HVAF sprayed coatings showed particle-like appearance of carbide phase whereas the HVOF sprayed coatings had a splat-like appearance. This was attributed to the difference in the processing conditions of the coatings.
- HVOF sprayed coatings exhibited coarser pore size than HVAF coatings, although their overall porosity content was comparable to HVAF coatings.

- XRD analysis of the coatings and feedstock confirmed similar phase composition and negligible decarburization/oxidation.
- HVAF coatings showed inferior wear resistance at 5 N than HVOF coatings. The particle-like surface morphology of HVAF coatings led to easier detachment of the carbide phase compared to splat-like morphology in HVOF coatings where the Ni-phase covered carbide phase resisted easier detachment.
- HVAF coatings showed superior wear performance than HVOF coatings at 10 N and 15 N load. Coarser sub-surface pores in the HVOF coating led to localized collapse of splats, resulting in higher wear rates for the HVOF coating than the HVAF coating.
- HVAF and HVOF coatings showed similar wear mechanisms, i.e., tribo-oxidation, abrasive wear (micro-cutting of Ni and Micro-cracking of  $\text{Cr}_3\text{C}_2$ ), adhesive wear, and carbide-pullout.

Based on the results, it can be concluded that  $\text{Cr}_3\text{C}_2$ -NiCr coatings comprising fine pores and substantially covered  $\text{Cr}_3\text{C}_2$  phase by the Ni-phase demonstrate a higher sliding wear resistance under different load conditions.

#### Declaration of Competing Interest

The authors declare that they have no known competing financial interests or personal relationships that could have appeared to influence the work reported in this paper.

#### Acknowledgments

The authors gratefully acknowledge NUCoP project (Energimyndigheten, Sweden, Dnr. 2018-003191, Project nr. P46393-1) for the financial support.

#### REFERENCES

- [1] Holmberg K, Erdemir A. Influence of tribology on global energy consumption, costs and emissions. *Friction* 2017;5(3):263–84. <https://doi.org/10.1007/s40544-017-0183-5>.
- [2] Anand VK, Aherwar A, Mia M, Elfakir O, Wang L. Influence of silicon carbide and porcelain on tribological performance of Al6061 based hybrid composites. *Tribol Int* 2020;151:106514. <https://doi.org/10.1016/j.triboint.2020.106514>.
- [3] Mehta J, Mittal VK, Gupta P. Role of thermal spray coatings on wear, erosion and corrosion behavior: a review. *J Appl Sci Eng* 2017;20(4):445–52. <https://doi.org/10.6180/jase.2017.20.4.05>.
- [4] Aranke O, Algenaid W, Awe S, Joshi S. Coatings for automotive gray cast iron brake discs: a review. *Coatings* 2019;9(9):552. <https://doi.org/10.3390/coatings9090552>.
- [5] Dev S, Aherwar A, Patnaik A. Preliminary evaluations on development of recycled porcelain reinforced LM-26/Al-Si10Cu3Mg1 alloy for piston materials. *Silicon* 2019;11(3):1557–73. <https://doi.org/10.1007/s12633-018-9979-9>.
- [6] Aherwar A, Patnaik A, Pruncu CI. Effect of B4C and waste porcelain ceramic particulate reinforcements on mechanical

- and tribological characteristics of high strength AA7075 based hybrid composite. *J Mater Res Technol* 2020;9(5):9882–94. <https://doi.org/10.1016/j.jmrt.2020.07.003>.
- [7] Kumar Sharma A, Bhandari R, Aherwar A, Pinca-Bretotean C. A study of fabrication methods of aluminum based composites focused on stir casting process. *Mater Today Proc* 2020;27:1608–12. <https://doi.org/10.1016/j.matpr.2020.03.316>.
  - [8] Chen H, Hutchings IM. Abrasive wear resistance of plasma-sprayed tungsten carbide–cobalt coatings. *Surf Coat Technol* 1998;107(2):106–14. [https://doi.org/10.1016/S0257-8972\(98\)00581-7](https://doi.org/10.1016/S0257-8972(98)00581-7).
  - [9] Baik KH, Kim JH, Seong BG. Improvements in hardness and wear resistance of thermally sprayed WC-Co nanocomposite coatings. *Mater Sci Eng A* 2007;449(451):846–9. <https://doi.org/10.1016/j.msea.2006.02.295>.
  - [10] Berghaus JO, Marple B, Moreau C. Suspension plasma spraying of nanostructured WC-12Co coatings. *J Therm Spray Technol* 2006;15(4):676–81. <https://doi.org/10.1361/105996306X147072>.
  - [11] De Boeck M, Kirsch-Volders M, Lison D. Cobalt and antimony: genotoxicity and carcinogenicity. *Mutat Res Mol Mech Mutagen* 2003;533(1):135–52. <https://doi.org/10.1016/j.mrfmmm.2003.07.012>.
  - [12] Suh M, Thompson CM, Brorby GP, Mittal L, Proctor DM. Inhalation cancer risk assessment of cobalt metal. *Regul Toxicol Pharmacol* 2016;79:74–82. <https://doi.org/10.1016/j.yrtph.2016.05.009>.
  - [13] van den Brink S, Kleijn R, Sprecher B, Tukker A. Identifying supply risks by mapping the cobalt supply chain. *Resour Conserv Recycl* 2020;156:104743. <https://doi.org/10.1016/j.resconrec.2020.104743>.
  - [14] Guilemany JM, Espallargas N, Fernández J, Suegama PH, Benedetti AV. High-velocity oxyfuel Cr<sub>3</sub>C<sub>2</sub>-NiCr replacing hard chromium coatings. *J Therm Spray Technol* 2005;14(3):335–41. <https://doi.org/10.1361/105996305X59350>.
  - [15] Espallargas N, Berget J, Guilemany JM, Benedetti AV, Suegama PH. Cr<sub>3</sub>C<sub>2</sub>-NiCr and WC-Ni thermal spray coatings as alternatives to hard chromium for erosion–corrosion resistance. *Surf Coat Technol* 2008;202(8):1405–17. <https://doi.org/10.1016/j.surfcoat.2007.06.048>.
  - [16] Bolelli G, Berger L-M, Börner T, Koivuluoto H, Matikainen V, Lusvarghi L, et al. Sliding and abrasive wear behaviour of HVOF- and HVOF-sprayed Cr<sub>3</sub>C<sub>2</sub>-NiCr hardmetal coatings. *Wear* 2016;358(359):32–50. <https://doi.org/10.1016/j.wear.2016.03.034>.
  - [17] Matikainen V, Bolelli G, Koivuluoto H, Sassatelli P, Lusvarghi L, Vuoristo P. Sliding wear behaviour of HVOF and HVOF sprayed Cr<sub>3</sub>C<sub>2</sub>-based coatings. *Wear* 2017;388(389):57–71. <https://doi.org/10.1016/j.wear.2017.04.001>.
  - [18] Hagino H, Oyama M, Sasaki S. Airborne brake wear particle emission due to braking and accelerating. *Wear* 2015;334(335):44–8. <https://doi.org/10.1016/j.wear.2015.04.012>.
  - [19] Houdková Š, Zahálka F, Kašparová M, Berger L-M. Comparative study of thermally sprayed coatings under different types of wear conditions for hard chromium replacement. *Tribol Lett* 2011;43(2):139–54. <https://doi.org/10.1007/s11249-011-9791-9>.
  - [20] Fedrizzi L, Rossi S, Cristel R, Bonora PL. Corrosion and wear behaviour of HVOF cermet coatings used to replace hard chromium. *Electrochim Acta* 2004;49(17):2803–14. <https://doi.org/10.1016/j.electacta.2004.01.043>.
  - [21] Picas JA, Forn A, Igartua A, Mendoza G. Mechanical and tribological properties of high velocity oxy-fuel thermal sprayed nanocrystalline CrC-NiCr coatings. *Surf Coat Technol* 2003;174(175):1095–100. [https://doi.org/10.1016/S0257-8972\(03\)00393-1](https://doi.org/10.1016/S0257-8972(03)00393-1).
  - [22] Liu X, Zhao X, Yang F. Room-temperature and high-temperature wear behaviors of as-sprayed and annealed Cr<sub>3</sub>C<sub>2</sub>-25NiCr coatings prepared by high velocity air-fuel spraying. *Coatings* 2020;10(11). <https://doi.org/10.3390/coatings10111090>.
  - [23] Määttä A, Kanerva U, Vuoristo P. Structure and tribological characteristics of HVOF coatings sprayed from powder BLENDS of Cr<sub>3</sub>C<sub>2</sub>-25NiCr and NiCrBSi alloy. *J Therm Spray Technol* 2011;20(1):366–71. <https://doi.org/10.1007/s11666-010-9579-8>.
  - [24] Gariboldi E, Rovatti L, Lecis N, Mondora L, Mondora GA. Tribological and mechanical behaviour of Cr<sub>3</sub>C<sub>2</sub>-NiCr thermally sprayed coatings after prolonged aging. *Surf Coat Technol* 2016;305:83–92. <https://doi.org/10.1016/j.surfcoat.2016.07.087>.
  - [25] Guilemany JM, Miguel JM, Vizcaíno S, Lorenzana C, Delgado J, Sánchez J. Role of heat treatments in the improvement of the sliding wear properties of Cr<sub>3</sub>C<sub>2</sub>-NiCr coatings. *Surf Coat Technol* 2002;157(2):207–13. [https://doi.org/10.1016/S0257-8972\(02\)00148-2](https://doi.org/10.1016/S0257-8972(02)00148-2).
  - [26] Kathuria YP. Some aspects of laser surface cladding in the turbine industry. *Surf Coat Technol* 2000;132(2):262–9. [https://doi.org/10.1016/S0257-8972\(00\)00735-0](https://doi.org/10.1016/S0257-8972(00)00735-0).
  - [27] Bienk EJ, Reitz H, Mikkelsen NJ. Wear and friction properties of hard PVD coatings. *Surf Coat Technol* 1995;76(77):475–80. [https://doi.org/10.1016/0257-8972\(95\)02498-0](https://doi.org/10.1016/0257-8972(95)02498-0).
  - [28] Rebenne HE, Bhat DG. Review of CVD TiN coatings for wear-resistant applications: deposition processes, properties and performance. *Surf Coat Technol* 1994;63(1):1–13. [https://doi.org/10.1016/S0257-8972\(05\)80002-7](https://doi.org/10.1016/S0257-8972(05)80002-7).
  - [29] Joshi S, Nylen P. Advanced coatings by thermal spray processes. *Technologies* 2019;7(4):79. <https://doi.org/10.3390/technologies7040079>.
  - [30] Tejero-Martin D, Rezvani Rad M, McDonald A, Hussain T. Beyond traditional coatings: a review on thermal-sprayed functional and smart coatings. *J Therm Spray Technol* 2019;28(4):598–644. <https://doi.org/10.1007/s11666-019-00857-1>.
  - [31] Baiamonte L, Björklund S, Mulone A, Klement U, Joshi S. Carbide-laden coatings deposited using a hand-held high-velocity air-fuel (HVOF) spray gun. *Surf Coat Technol* 2021;406:126725. <https://doi.org/10.1016/j.surfcoat.2020.126725>.
  - [32] Lu H, Shang J, Jia X, Li Y, Li F, Li J, et al. Erosion and corrosion behavior of shrouded plasma sprayed Cr<sub>3</sub>C<sub>2</sub>-NiCr coating. *Surf Coat Technol* 2020;388:125534. <https://doi.org/10.1016/j.surfcoat.2020.125534>.
  - [33] Chhabra P, Kaur M. Wear and friction characteristics of atmospheric plasma sprayed Cr<sub>3</sub>C<sub>2</sub>-NiCr coatings. *Tribol Mater Surf Interfaces* 2020;14(3):177–92. <https://doi.org/10.1080/17515831.2020.1720383>.
  - [34] Mahade S, Björklund S, Govindarajan S, Olsson M, Joshi S. Novel wear resistant carbide-laden coatings deposited by powder-suspension hybrid plasma spray: characterization and testing. *Surf Coat Technol* 2020;126147. <https://doi.org/10.1016/j.surfcoat.2020.126147>.
  - [35] Toma F-L, Potthoff A, Berger L-M, Leyens C. Demands, potentials, and economic aspects of thermal spraying with suspensions: a critical review. *J Therm Spray Technol* 2015;24(7):1143–52. <https://doi.org/10.1007/s11666-015-0274-7>.
  - [36] Bolelli G, Berger L-M, Borner T, Koivuluoto H, Lusvarghi L, Lyphout C, et al. Tribology of HVOF- and HVOF-sprayed WC-10Co4Cr hardmetal coatings: a comparative assessment. *Surf Coat Technol* 2015;265:125–44. <https://doi.org/10.1016/j.surfcoat.2015.01.048>.
  - [37] Garfias Bulnes A, Albaladejo Fuentes V, Garcia Cano I, Dosta S. Understanding the influence of high velocity thermal spray techniques on the properties of different



- anti-wear WC-based coatings. *Coatings* 2020;10(12). <https://doi.org/10.3390/coatings10121157>.
- [38] Jacobs L, Hyland MM, De Bonte M. Comparative study of WC-cermet coatings sprayed via the HVOF and the HVOF Process. *J Therm Spray Technol* 1998;7(2):213–8. <https://doi.org/10.1361/105996398770350954>.
- [39] Matikainen V, Koivuluoto H, Vuoristo P. A study of Cr<sub>3</sub>C<sub>2</sub>-based HVOF- and HVOF-sprayed coatings: abrasion, dry particle erosion and cavitation erosion resistance. *Wear* 2020;446(447):203188. <https://doi.org/10.1016/j.wear.2020.203188>.
- [40] Mahade S, Mulone A, Björklund S, Klement U, Joshi S. Novel suspension route to incorporate graphene nano-platelets in HVOF-sprayed Cr<sub>3</sub>C<sub>2</sub>-NiCr coatings for superior wear performance. *J Mater Res Technol* 2021;13:498–512. <https://doi.org/10.1016/j.jmrt.2021.04.096>.
- [41] Schneider CA, Rasband WS, Eliceiri KW. NIH Image to ImageJ: 25 years of image analysis. *Nat Methods* 2012;9(7). <https://doi.org/10.1038/nmeth.2089>.
- [42] Tillmann W, Vogli E, Baumann I, Kopp G, Weihs C. Desirability-based multi-criteria optimization of HVOF spray experiments to manufacture fine structured wear-resistant 75Cr<sub>3</sub>C<sub>2</sub>-25(NiCr20) coatings. *J Therm Spray Technol* 2010;19(1):392–408. <https://doi.org/10.1007/s11666-009-9383-5>.
- [43] Li M, Christofides PD. Modeling and control of high-velocity oxygen-fuel (HVOF) thermal spray: a tutorial review. *J Therm Spray Technol* 2009;18(5):753. <https://doi.org/10.1007/s11666-009-9309-2>.
- [44] Mahade S, Baiamonte L, Sadeghimeresht E, Björklund S, Marra F, Joshi S. Novel utilization of powder-suspension hybrid feedstock in HVOF spraying to deposit improved wear and corrosion resistant coatings. *Surf Coat Technol* 2021;412:127015. <https://doi.org/10.1016/j.surfcoat.2021.127015>.
- [45] Mahade S, Aranke O, Björklund S, Dizdar S, Awe S, Mušálek R, et al. Influence of processing conditions on the microstructure and sliding wear of a promising Fe-based coating deposited by HVOF. *Surf Coat Technol* 2021;409:126953. <https://doi.org/10.1016/j.surfcoat.2021.126953>.
- [46] Ye HZ, Li DY, Eadie RL. Influences of porosity on mechanical and wear performance of pseudoelastic TiNi-matrix composites. *J Mater Eng Perform* 2001;10(2):178–85. <https://doi.org/10.1361/105994901770345196>.
- [47] Mahade S, Venkat A, Curry N, Leitner M, Joshi S. Erosion performance of atmospheric plasma sprayed thermal barrier coatings with diverse porosity levels. *Coatings* 2021;11(1). <https://doi.org/10.3390/coatings11010086>.
- [48] Kumar N, Mahade S, Ganvir A, Joshi S. Understanding the influence of microstructure on hot corrosion and erosion behavior of suspension plasma sprayed thermal barrier coatings. *Surf Coat Technol* 2021;419:127306. <https://doi.org/10.1016/j.surfcoat.2021.127306>.
- [49] Matthews S, James B, Hyland M. The role of microstructure in the mechanism of high velocity erosion of Cr<sub>3</sub>C<sub>2</sub>-NiCr thermal spray coatings: part 1 — as-sprayed coatings. *Surf Coat Technol* 2009;203(8):1086–93. <https://doi.org/10.1016/j.surfcoat.2008.10.005>.
- [50] Qin E, Wang B, Li W, Ma W, Lu H, Wu S. Optimized microstructure and properties of Cr<sub>3</sub>C<sub>2</sub>-NiCr cermet coating by HVOF/laser hybrid processing. *J Therm Spray Technol* 2019;28(5):1072–80. <https://doi.org/10.1007/s11666-019-00877-x>.
- [51] Quinn GD, Bradt RC. On the vickers indentation fracture toughness test. *J Am Ceram Soc* 2007;90(3):673–80. <https://doi.org/10.1111/j.1551-2916.2006.01482.x>.
- [52] Zhou D, Guillon O, Vaßen R. Development of YSZ thermal barrier coatings using axial suspension plasma spraying. *Coatings* 2017;7(8):120. <https://doi.org/10.3390/coatings7080120>.
- [53] Murray JW, Leva A, Joshi S, Hussain T. Microstructure and wear behaviour of powder and suspension hybrid Al<sub>2</sub>O<sub>3</sub>-YSZ coatings. *Ceram Int* 2018;44(7):8498–504. <https://doi.org/10.1016/j.ceramint.2018.02.048>.
- [54] Ramachandran CS, Balasubramanian V, Ananthapadmanabhan PV. Erosion of atmospheric plasma sprayed rare earth oxide coatings under air suspended corundum particles. *Ceram Int* 2013;39(1):649–72. <https://doi.org/10.1016/j.ceramint.2012.06.077>.
- [55] Mahade S, Zhou D, Curry N, Markocsan N, Nylén P, Vaßen R. Tailored microstructures of gadolinium zirconate/YSZ multi-layered thermal barrier coatings produced by suspension plasma spray: durability and erosion testing. *J Mater Process Technol* 2019;264:283–94. <https://doi.org/10.1016/j.jmatprotec.2018.09.016>.
- [56] Venturi F, Rance GA, Thomas J, Hussain T. A low-friction graphene nanoplatelets film from suspension high velocity oxy-fuel thermal spray. *AIP Adv* 2019;9(2):25216. <https://doi.org/10.1063/1.5089021>.
- [57] Venturi F, Pulsford J, Hussain T. A novel approach to incorporate graphene nanoplatelets to Cr<sub>2</sub>O<sub>3</sub> for low-wear coatings. *Mater Lett* 2020;276:128283. <https://doi.org/10.1016/j.matlet.2020.128283>.
- [58] Vashishtha N, Sapate SG, Gahlot JS, Bagde P. Effect of tribo-oxidation on friction and wear behaviour of HVOF sprayed WC-10Co-4Cr coating. *Tribol Lett* 2018;66(2):56. <https://doi.org/10.1007/s11249-018-1006-1>.
- [59] Vashishtha N, Sapate SG. Abrasive wear maps for high velocity oxy fuel (HVOF) sprayed WC-12Co and Cr<sub>3</sub>C<sub>2</sub>-25NiCr coatings. *Tribol Int* 2017;114:290–305. <https://doi.org/10.1016/j.triboint.2017.04.037>.
- [60] Ghabchi A. *Wear resistant carbide-based thermal sprayed coatings: process, properties, mechanical degradation and wear*. U.S: Stony Brook University; 2011.